Left-Ventricle myocardium segmentation using a Coupled Level-Set with A-Priori knowledge

M. Lynch *, O. Ghita P. F. Whelan

Vision Systems Group, Dublin City University, Dublin 9, Ireland

Abstract

This paper presents a coupled level-set segmentation of the myocardium of the left ventricle of the heart using *a priori* information. From a fast marching initialisation, two fronts representing the endo-cardium and epi-cardium boundaries of the left ventricle are evolved as the zero level-set of a higher dimension function. We introduce a novel and robust stopping term using both gradient and region-based information. The segmentation is supervised both with a coupling function and using a probabilistic model built from training instances. The robustness of the segmentation scheme is evaluated by performing a segmentation on four unseen data-sets containing high variation and the performance of the segmentation is quantitatively assessed.

Key words: Keywords: Level-set, segmentation, cardiac, left-ventricle, coupled, *a priori* knowledge

* Corresponding author.
Email address: lynchm@eeng.dcu.ie (M. Lynch).

1 Introduction

Early identification of myocardium dysfunction through quantitative analysis, permits a reliable and fast diagnosis of heart diseases. Such quantitative functions include left ventricle ejection fraction, left ventricle myocardium thickening over the cardiac cycle and left ventricle myocardium mass. To evaluate these measures, accurate delineation of the left ventricle cavity and left ventricle cardiac muscle is required.

Advanced imaging techniques in Magnetic Resonance Imaging (MRI) have allowed for the imaging of the heart muscle at increasing spatial and temporal resolutions. Multisection multiphase short-axis cardiac MR images are the most suitable to assess left ventricle function without drawing any assumptions about left ventricle geometry [1]. Traditional methods of quantitative analysis required the manual delineation of the myocardium. This has become increasingly time consuming with the extra data now available from a single MRI examination. Therefore an automatic segmentation of the left ventricle myocardium is desired. This issue has been previously addressed in literature and the developed methods can be classified into region-based and boundary finding approaches.

Region-based methods are used to segment the image, commonly using no *a priori* information. The most basic form of region-based segmentation is thresholding. Thresholding requires a high degree of supervision, high differentiation between the object being segmented and the background and may require some additional post processing. More complex statistical region-based methods like clustering, collect pixels of similar intensities to create a segmen-

tation of structures in the image [2]. However, in some cases the distributions of one structure may locally overlap with those from another structure rendering intensity-based segmentation techniques unusable.

Boundary finding algorithms like snakes [3], aspire to deform a local boundary curve and come to rest on the high frequency data in an image, corresponding to edges. Such algorithms are sensitive to initialisation, local minima and leaking through boundaries of low gradient.

Active Shape Models (ASMs) proposed by Cootes [4] use a statistical model built up from a training set of segmented objects to delineate the desired shape. The model is compiled and then compressed, commonly using Principal Component Analysis (PCA). ASMs have become a prominent tool in the segmentation of the left ventricle [5, 6]. It is also worth noting that the accuracy of the segmentation relies heavily on the amount and variation of images in the training set.

Active Appearance Models (AAMs) [4] are an extension to ASMs which use the texture variation in the training set in the compressed PCA. This method alleviates the problems associated with the ASMs in areas of low gradients. Stegmann [7] showed how these active appearance models could be applied to analyse short axis MR images of the heart. Mitchell [8] addresses the problems that AAMs have with attaching the model with the gradient information. A hybrid approach is taken which combines ASMs and AAMs. Lelieveldt [9] introduces a time factor into his Active Appearance Motion Models (AAMMs) and minimises the appearance-to-target differences.

Level-set methods for segmentation (also called Geodesic Active Contours) were first introduced by Osher and Sethian in 1988 [10] following previous

work in Sethian's Ph.D. thesis [11] on flame propagation. The theory behind this boundary-based segmentation is largely based on work in partial differential equations and the propagation of fronts under intrinsic properties such as curvature [12]. The deformation of the level set is seen as a gradient flow to a state of minimal energy providing the object to be segmented has clearly identifiable boundaries [13,14]. By extending the dimensionality of the problem to N + 1, where N is the initial dimension of the problem, some advantageous properties can be exploited. These include level-sets ability to deal with local deformations like shape corners, changes in topology and multi-component structures. Such qualities lend themselves well in the field of medical image segmentation where the biological structures split and merge through the volume. In our case, this is useful when separating the papillary muscles from the blood pool. Malladi [15, 16] showed how level-set algorithm could be applied for enhancement and shape recovery in medical images. An extension of Malladi's work, performed by Niessen [17] uses a more diffusive propagation term to increase the influence of the stopping term.

Zeng et al. [18] first introduced the idea of coupled level sets for segmentation of the cortex of the brain. The coupled level set can use the constant thickness or distance between the level-sets as a constraint to avoid spilling or over segmentation. The ideas introduced by Zeng were extended by Paragios [19] who applied a similar coupling constraint for the segmentation of the myocardium of the heart.

Leventon [20] introduced *a priori* knowledge by building an *a priori* model that was embedded in a level set formalisation and evaluating its modes of variation using PCA analysis. Paragios [21] extended this idea by using intensity based probability knowledge about the left ventricle blood pool and

myocardium and incorporating this into the segmentation process.

The method described in this paper performs a coupled level-set segmentation of the left ventricle myocardium. We increase robustness by incorporating textual information into the stopping term. This segmentation is supervised by incorporating *a priori* knowledge into the evolution and applying this information in a global sense to avoid leaking and selecting false local minima. The *a priori* model is a probability function derived from manually segmented heart images which biases results towards a training set. Due to the low signal to noise ration(SNR) present in MRI scans, region based information is included in the deformation, which gives improved robustness in the segmentation of a wide variation of cardiac morphologies. Analysis of point-to-curve errors, reproducibility plots and correlation results are provided on data-sets of the heart and compared against manual delineation.

2 Method

A level-set segmentation is performed to robustly segment the myocardium of the left ventricle of the heart. Level-set segmentation involves a deformable curve or surface evolving under gradient information and the intrinsic curvature. To overcome limitations with gradient based stopping terms, we introduce a region based term to the stopping function to increase robustness. To further control the evolution, two additional features have being applied. Firstly, a coupled level-set is introduced, representing the endo- and epi-cardium boundary of the left ventricle. These two level-sets interact with each other through the evolution using a coupling function. This prohibits the endo-cardium boundary joining with the epi-cardium boundary and also restricts

the epi-cardium boundary spilling where there is no gradient information available. The second feature to be added to the evolution is *a priori* information, obtained from manual segmentations of the endo- and epi-cardium boundaries. This controls the evolution to bias manually defined shapes of the left ventricle muscle.

2.1 Level-Set Formulation Background

The fundamental objective behind level-sets is to track a closed interface $\Gamma(t)$, for which $\Gamma(t) : [0, \infty) \rightarrow R^N$, as it evolves in the data space. The interface is represented by a curve in 2D and a surface in 3D or the set of points that are on the boundaries of the region of interest Ω. Caselles et al [13] formalised the minimization of the classic energy function used in snake evolution for the extension to levelset theory.

$$\min \int g(|\nabla I(\Gamma(s))|, I_\sigma)|\Gamma'(s)|ds \tag{1}$$

We reformulate the stopping term to include the gradient (∇I) and region changes (I_σ) at that position. This improves segmentation by enforcing homogeneity within the region Ω being segmented and is illustrated in Figures 1 and 2. ∇I is the gradient value measured across a six connected 3D neighborhood. I_σ is a measure of the change in texture and is calculated by firstly measuring the mean and variance of the voxels chosen during the initialisation stage.

$$g = \frac{1}{1 + \frac{\nabla I}{I_\sigma}} \tag{2}$$

Level-set theory aims to exchange the Lagranian formalisation and replace it with Eulerian, initial valued partial differential equation evolution. From [13]

it can be shown that the Euler-Lagrange gives a minimizing curve that is of the form.

$$\frac{d}{dt}\Gamma(s) = g(|\nabla I|)\kappa\vec{n} - (\nabla g \cdot \vec{n})\vec{n} \tag{3}$$

The term $\nabla g \cdot \vec{n}$ is a naturally accuring attraction force vector normal to the surface and κ is the curvature term. By representing the boundary as the zero level set instance of a higher dimensional function ϕ, the effects of curvature can be easily incorporated. ϕ is represented by the continuous Lipschitz function $\phi(s, t = 0) = \pm d$, where d is the signed distance from position s to the initial interface Γ_0. The Lipschitz condition implies that the function has a bounded first derivative. The distance is given a positive sign outside the initial boundary ($D\ \Omega$), a negative sign inside the boundary ($\Omega \setminus \partial\Omega$) and zero on the boundary ($\partial\Omega$).

$$\phi(s) = \begin{cases} -d & \forall s \in \Omega \setminus \partial\Omega \\ 0 & \forall s \in \partial\Omega \\ +d & \forall s \in R^n \setminus \Omega \end{cases} \tag{4}$$

From this definition of ϕ, intrinsic properties of the front can be easily determined, like the normal $\vec{n} = \pm\frac{\nabla\phi}{|\nabla\phi|}$ and the curvature $\kappa = \nabla \cdot \frac{\nabla\phi}{|\nabla\phi|}$.

In the segmentation scheme we would like to add a non-zero internal advection or ballooning force, c , to the evolution, to evolve the either outward ($c = 1$) or inward ($c = -1$). β and ϵ are independent user defined parameters controlling the effects of attraction to gradients and curvature respectively.

$$\frac{\partial\phi}{\partial t} = g(I)(c + \epsilon\kappa)|\nabla\phi| + \beta(\nabla g \cdot \nabla\phi) \tag{5}$$

2.1.1 Determination of the stopping term

To illustrate the improved performance of the advanced stopping term, the following phantom images were created and tested. Two situations are described, the first where low gradient information is present between two regions and the second where the grayscale difference between two regions was low. The stopping term, as defined in Equation 2, uses a combination of the gradient and change in texture. The change in texture (I_σ) is calculated after the initialisation with the fast marching algorithm described in Section 2.4. Within the initialised region the mean μ and variance σ of the voxels are calculated. From these values, a Gaussian is constructed and the $I_\sigma(s)$ is calculated as,

$$I_\sigma(s) = \frac{1}{2\pi\sigma^2} e^{\frac{(x-\mu)^2}{2\sigma^2}} \tag{6}$$

where x is the value of the voxel at each position s in the image. The value of I_σ is normalised between 0-1.

The user defined parameters ϵ and β represent the influence of the curvature and attraction to gradient on the evolving boundary. In the following tests, we want to evaluate the influence of the improved stopping term, so the value of ϵ is given less significance to reduce the influence of curvature on the evolution. In the segmentation of the left-ventricle boundaries, the value of ϵ is given a higher significance as we know the boundaries approximate circles. Similarly, β controls the attraction of the level-set boundary to gradients that are normal to the curve. Again, this value is given a reduced weighting in the proceeding tests. The results shown in Figures 1 and 2 demonstrate the improved robustness against boundary leaking between regions.

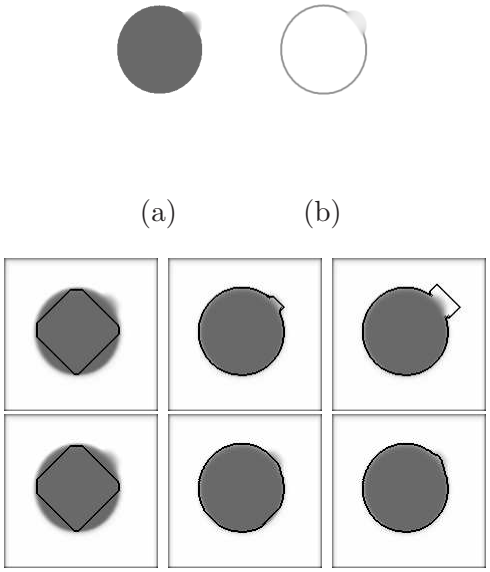

Fig. 1. The original phantom image with a diffused segment (a) and Sobel edge image (b). The second row shows the evolution with the existing $g = \frac{1}{1+\nabla I}$ at iteration 0, 25 and 50 while the third row shows the evolution with our proposed approach where $g = \frac{1}{1+\frac{\nabla I}{I_\sigma}}$ at iteration 0, 25 and 50.

2.2 Coupling Force

To further control the level-set evolution we employ a coupling function between two level-sets. The coupling adds an extra constraint by introducing a second level-set that is dependent on the first and coupling the level-sets with an inhibitor function, which allows the curve to change direction of growth. This is achieved without any extra computational expense as the distance between any point to the level-set boundary is the value of ϕ at that point, see Equation 4. The piecewise inhibitor function, which is used as the interaction between the two level-sets, is defined below, where d is the preferred distance between the curves and w controls the slope between inward and outward growth. The result $\eta_2(\phi_1)$ changes value from +1 to -1, which changes the

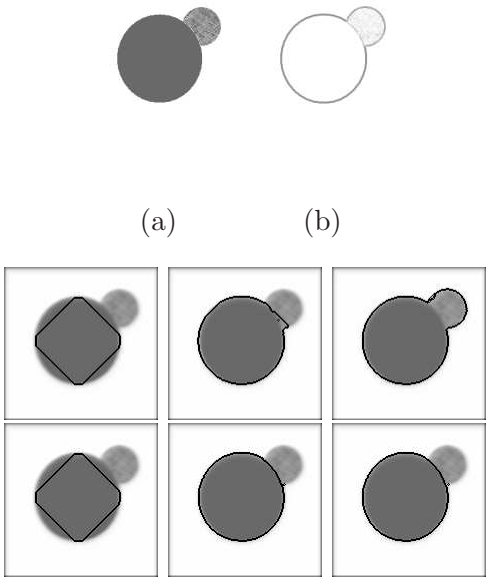

Fig. 2. The original phantom image with a close region (a) and Sobel edge image (b). The second row shows the evolution with the existing $g = \frac{1}{1+\nabla I}$ at iteration 0, 25 and 50 while the third row shows the evolution with our proposed approach where $g = \frac{1}{1+\frac{\nabla I}{I_\sigma}}$ at iteration 0, 25 and 50.

direction of the evolution for ϕ_2 between inwards and outwards. In practice the values of d and w are taken from the scaled *a priori* model.

$$\eta_2(\phi_1) = \begin{cases} -1 & \text{for } \phi_1(s) < -d - w \\ |\sqrt[3]{\frac{\phi_1(s)-d}{w}}| & \text{for } -d - w < \phi_1(s) < d + w \\ 1 & \text{for } \phi_1(s) > d + w \end{cases} \tag{7}$$

For this segmentation scheme, it is assumed that the gradient between the blood pool and the endo-cardium boundary is significantly high to halt the evolution of the level-set, also it is known that in some cases there is little or no gradient information between the epi-cardium boundary and the lungs or liver. Therefore, the level-set segmenting the epi-cardium boundary is controlled by

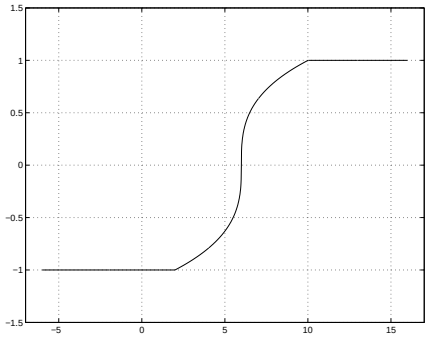

Fig. 3. Graph of the inhibitor function where the values of $d = 6$ and $w = 4$.

the endo-cardium level-set using the inhibitor function described.

2.3 Introducing Priors

A priori information is incorporated with a probability density function (PDF), which is defined as $P(s) = \int f(s)\ ds$. The model is built from a set of hand segmented boundaries, a probable density function is created of both the endo-cardium and epi-cardium boundaries that are then interpolated in the z direction, scaled and aligned in the xy direction.

The PDF is constructed by aligning the binary manually segmented boundary images and summing the boundary elements. This is done for both the endo-cardium boundary and the epi-cardium boundary. It is incorporated into the evolution in a global context, after each iteration the value ρ_t is evaluated as,

$$\rho_t = \sum \phi(t)_s * P_s \tag{8}$$

where $\phi(t)_s$ is the value of ϕ at time t at the position s and P_s is the probability density at position s.

In order to obtain the full evolution equation for the level-set we have to incor-

porate both the coupling function and the *a priori* knowledge into Equation 5. Firstly, the output from the coupling function is either 1 or -1 and we want it to change the direction of the curve evolution. From Equation 5 we can see that the advection force defines the direction of the evolution, therefore we incorporate the coupling function by multiplying it with the advection force c. The *a priori* is designed to disregard inappropriate gradients and give significance only to gradients that are situated close to previously manually segmented boundaries. For this reason, we incorporate the *a priori* information in the attraction term from Equation 5. Thus, the complete evolution for the coupled level-set is defined as,

$$\phi_{t+1} = \phi_t + g(I)(c\eta + \epsilon\kappa)|\nabla\phi| + \frac{\beta}{1+\tilde{\rho}_t}(\nabla g \cdot \nabla\phi) \tag{9}$$

where η is the result of the coupling function between the level-sets and is defined in Equation 7 and ρ_t is the *a priori* knowledge and is defined in Equation 8.

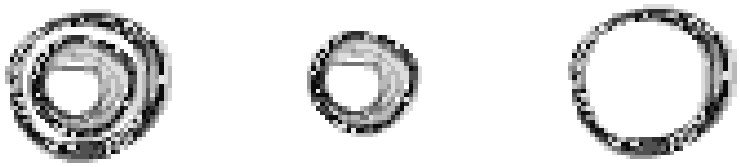

(a) (b) (c)

Fig. 4. Images show the probability density functions from a priori hand segmented images. Figure *(a)* shows the combined contours while *(b)* and *(c)* show the endo- and epi-cardium boundaries respectively. Darker gray tone defines a higher probability of the boundaries.

2.4 Initialisation

To counteract the 'myopic' characteristics of these deformable models, the initialisation process is very influential and is performed as follows. Firstly, it is known that the endocardium boundary can be characterised by the high contrast between the blood and the heart muscle in standard (TruFISP) cine imaging of the heart. This characteristic is used when a fast marching algorithm is applied to find a fast efficient initialisation for the blood following the manual insertion of a seed point. The fast marching approach is driven by a force $F_s = e^{-\alpha \nabla I_s}$, which has a diffusive effect aimed at halting the fronts progress at regions of high gradient. This fast-marching approach falls short of the gradient defining the transition from blood to muscle. Therefore the contour found by the fast marching algorithm is used as the initial curve of the level-set algorithm to find the endocardium boundary. The results from the Fast Marching initialisation are illustrated in Figure 5.

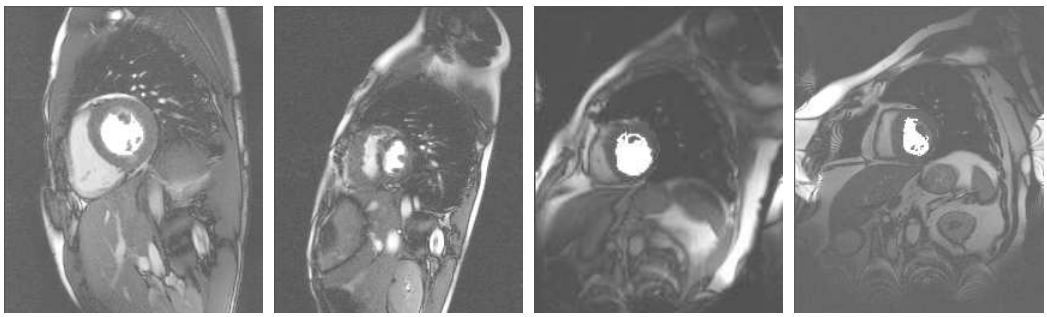

Fig. 5. Results show the initialisation (marked in white) from a seeded Fast Marching algorithm. The method was applied to perform a robust initial estimate of left ventricle cavity of the heart on four separate datasets displaying a high variability of left ventricle shape.

To find the epi-cardial boundary the endocardium initialisation is dilated slightly and the inner gradients are masked. Both curves are given a posi-

tive advection force to propagate outwards. It is known that both the endo- and epi-cardium boundaries of the left ventricle are approximately circular, therefore the ϵ is given a high significance in the evolution. High curvature constraints, the distance inhibitor and the *a priori* constraints all act to limit the epi-cardium front from joining the inner front or spilling in areas of low gradient, like the liver or the lungs.

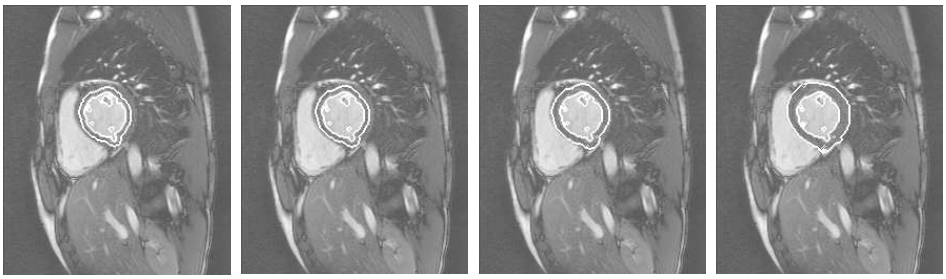

(a) (b) (c) (d)

Fig. 6. The images above show evolution of the front at four different iterations *(a)* $iteration = 0$, *(b)* $iteration = 5$, *(c)* $iteration = 10$ and *(d)* $iteration = 15$.

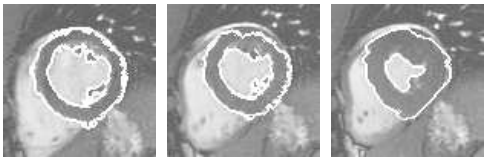

(a) (b) (c)

Fig. 7. Segmentation results of the same slice at three separate phases through the hearts cycle, *(a)* end-diastolic, *(b)* mid-diastolic and *(c)* end-systolic.

3 Results

In order to assess the performance of the segmentation, the results were compared against those obtained by manual segmentation of the endo and epi-

cardium boundaries. The algorithm is applied to four unseen datasets (see figure 8) with a high variation between datasets to assess the robustness when using the coupling function and the *a priori* model. The datasets have a variation in pixel spacing (1.1-2.3mm/pixel) so all error measurements are given in pixels. Table 1 represents the average, root mean square and variation of the point to curve error for both the endo-cardium boundary and the epi-cardium boundary.

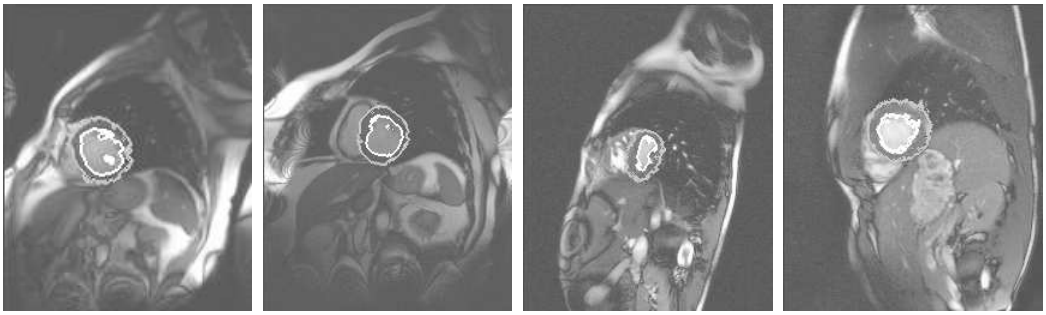

(a) (b) (c) (d)

Fig. 8. The images above show the segmentation using our method on the four previously unseen datasets.

	Point-to-Curve Error	
	Endocardium	Epicardium
Average	0.477	1.149
Root Mean Square	0.839	1.649
Standard Deviation	0.683	1.157

Table 1

Point-to-curve errors between manually segmented data and our method.

The results were then assessed in 2D using the areas enclosed in the endo and epi-cardium boundaries, see Figures 9 and 10. The results are displayed in

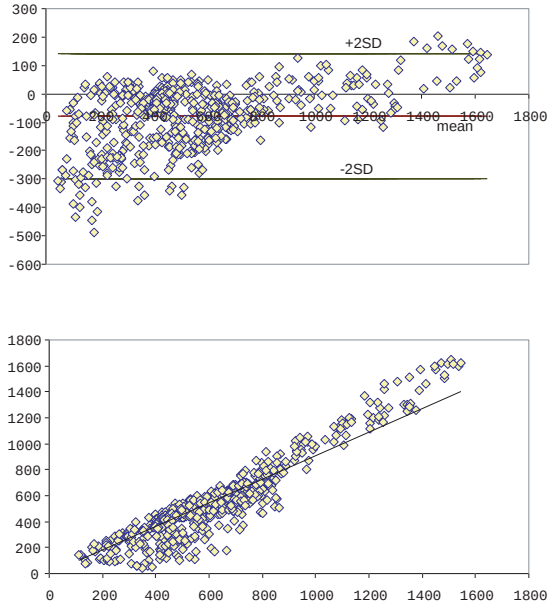

Fig. 9. The linear plot and Bland-Altman plot of the automatic segmentation against the manual segmentation for the endocardium for all datasets shown in Figure 8.

linear regression plots and in Bland-Altman [22] plots to assess reproducibility. The high gradient information present between the myocardium and the blood pools plays a crucial role in the accurate segmentation of the endocardium which yields a correlation factor of 0.86. To maintain the generality of this approach the parameters were unchanged for all datasets assessed. The correlation factor for the epi-cardium areas regression is 0.85. The higher than expected error illustrated in the Bland-Altman plots for figures 9 and 10 can be explained with the high variation of the datasets, in particular see Figure 8(c). To illustrate the influence of this dataset on the results, the dataset was removed and the results evaluated again. With this dataset removed (11% of the total number of images) the regression values increase to 0.89 and 0.87 for the endo-cardium and epi-cardium boundary respectively.

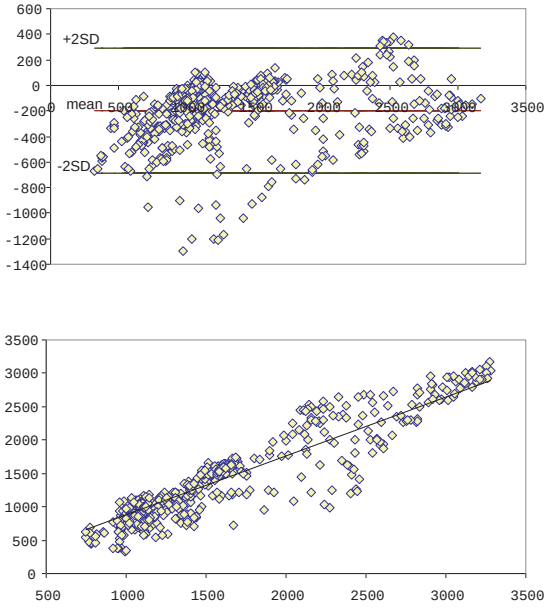

Fig. 10. The linear plot and Bland-Altman plot of the automatic segmentation against the manual segmentation for the epicardium for all datasets shown in Figure 8.

4 Conclusions and Future Work

The qualitative and quantitative results presented in this paper proves the validity of our coupled level-set method for cardiac myocardium segmentation. This paper describes a novel level-set segmentation where the evolution of the coupled fronts are dependent on both a coupling function and a model trained on real data. An improved stopping term is introduced that is dependent on both gradient and region information.

Positive aspects of the method include the accurate segmentation of the boundaries of the heart. Such a boundary based segmentation can give more accurate results than model fitting approaches, especially in the presence of pathologies. Improved robustness is achieved by using a coupled level-set approach. The method is constrained to limit over segmentation using both a distance

inhibitor and is predisposed to replicate expert manual segmentations.

Using the probabilities obtained from the PDF of the training set, our method addresses the limitation of model based approaches where there is a tradeoff between accuracy and generality. In these approaches, strengthening the *a priori's* influence on the evolution may result in loss of segmentation detail, patient abnormalities, muscle dysfunction etc. Investigating ways of improving accuracy without removing generality are part of our plans to further develop the method.

References

[1] B. P. F. Lelieveldt, R. J. van der Geest, H. J. Lamb, H. W. M. Kayser, and J. H.C Reiber. Automated observer-independent acquisition of cardiac short-axis MR images: A pilot study. *Radiology*, 221(2):537–542, 2001.

[2] A. Pednekar, I. A. Kakadiaris, and U. Kurkure. Adaptive fuzzy connectedness-based medical image segmentation. In *Indian Conference on Computer Vision, Graphics and Image Processing 2002*, Ahmedabad, India, December 2002.

[3] M. Kass, A. Witkin, and D. Terzopoulos. Snakes: Active Contour Models. *International Journal of Computer Vision*, 1(4):321–331, 1988.

[4] T. F. Cootes, G. J. Edwards, and C. J. Taylor. Active appearance models. *Lecture Notes in Computer Science*, 1407:484–498, 1998.

[5] G. Hamarneh and T. Gustavsson. Combining Snakes and Active Appearance Shape Models for Segmenting the Human Left Ventricle in Echocardiographic Images. *IEEE Computers in Cardiology*, 27:115–118, 2000.

[6] M. Rogers and J. Graham. Robust Active Shape Model Search. In *Proceedings of the 7th European Conference on Computer Vision*, pages 517–530, May 2002.

[7] M. B. Stegmann and H. B. W. Larsson. Motion-Compensation of Cardiac Perfusion MRI Using a Statistical Texture Ensemble. In *Functional Imaging and Modelling of the Heart (FIMH'03)*, pages 151–161, Lyon, France, June 2003.

[8] S. C. Mitchell, B. P. F. Lelieveldt, R. J. van der Geest, H. G. Bosch, J. H. C. Reiber, and M. Sonka. Multistage Hybrid Acive Appearance Model Matching: Segmentation of Left Ventricles in Cardiac MR Images. *IEEE Transactions on Medical Imaging*, 2001.

[9] J. G. Bosch, S. C. Mitchell, B. P. F. Lelieveldt, F. Nijland, O. Kamp, M. Sonka, and J.H.C. Reiber. Automatic segmentation of echocardiographic sequences by active appearance motion models. *IEEE Transactions on Medical Imaging*, 21(11), 2002.

[10] S. Osher and J. A. Sethian. Fronts propagating with curvature-dependent speed: Algorithms based on Hamilton-Jacobi formulations. *Journal of Computational Physics*, 79:12–49, 1988.

[11] J. A. Sethian. *An Analysis of Flame Propagation.* PhD thesis, University of California, Dept. of Mathematics, University of California, Berkeley, CA, USA, 1982.

[12] J. A. Sethian. A marching level set method for monotonically advancing fronts. In *Proceedings of the National Academy of Sciences*, volume 93, 1996.

[13] V. Caselles, R. Kimmel, and G. Sapiro. Geodesic active contours. *Int. J. Comput. Vision*, 22(1):61–79, 1997.

[14] V. Caselles, F. Catté, T. Coll, and F. Dibos. A geometric model for active contours in image processing. *Numerische Mathematik*, 66(1):1–31, October 1993.

[15] R. Malladi, J. A. Sethian, and B. C. Vermuri. Shape modeling with front propagation: A level set approach. *IEEE Transactions on Pattern Analysis and Machine Intelligence*, 17:158–175, 1995.

[16] R. Malladi and J. A. Sethian. Level set methods for curvature flow, image enhancement, and shape recovery in medical images. In *Proc. of Conf. on Visualization and Mathematics*, Berlin, Germany, June 1997.

[17] W. J. Niessen, B. M. ter Haar Romeny, and M. A. Viergever. Geodesic deformable models for medical image analysis. *Transactions on Medical Imaging*, 17(4):634–642, 1998.

[18] X. Zeng, L. H. Staib, R. T. Schultz, and J. S. Duncan. Segmentation and measurement of the cortex from 3D MR images. In *Medical Image Computing and Computer Asssisted Intervention, MICCAI*, October 1998.

[19] N. Paragios. A variational approach for the segmentation of the left ventricle in cardiac image analysis. *International Journal of Computer Vision*, 50(3):345–362, 2002.

[20] M. E. Leventon, W. E. L. Grimson, and O. Faugeras. Statistical shape influence in geodesic active contours. In *Proceedings of Computer Vision and Pattern Recognition*, 2000.

[21] N. Paragios. A level set approach for shape-driven segmentation and tracking of the left ventricle. *IEEE Transactions on Medical Imaging*, 22(6):773–776, June 2003.

[22] J. M. Bland and D. G. Altman. Statiscal methods for assessing agreement between two methods of clinical measurements. *Lancet*, 1(8476):307–310, 1986.